A Thermal Imaging Methodology To Study Evaporation Kinetics in Mine Tailings

Josée Maurais[1]*, Étienne Beaumont[1], Joanick Bourret[1], Emrik Dauphinais[1], Nicolas-Alexandre Bouchard[2] and Patrick Ayotte[1]

[1]Département de chimie, Université de Sherbrooke, Sherbrooke, J1K 2R1, CANADA

[2]Rio Tinto Alcan International Limited, 1955 boul. Mellon, Jonquière, G7S 4L2, CANADA

1

19   ABSTRACT

20   Predicting why, how, and when mine tailings disposal sites become prone to dust scattering events

21   is often hampered by our limited understanding of the factors that affect the drying rates from their

22   surface layers. As a case study, thermal imaging is demonstrated here to be a valuable tool to

23   study the evaporation mechanisms and rates from bauxite residues as a function of their thickness

24   and physicochemical properties, as well as environmental conditions.   These investigations reveal

25   their that late stage drying rates are limited by gas phase diffusion through the interstitial air within

26   their internal microporosity. The smallness of the effective diffusion coefficient indicates that

27   water adsorption on bauxite residues surfaces is the dominant phenomenon responsible for their

28   slow water vapour transport kinetics, a phenomenon that ultimately controls their late stage drying

29   rates, that is when dust scattering is most likely to occur. As such, application of this thermal

30   imaging methodology in the field may also contribute to improve the accuracy of risk assessment

31   protocols, support intervention and mitigation strategies, underpin optimization efforts for mining

32   residues management, and improve forecasting of fugitive dust emissions from mine tailings by

33   enabling more accurate predictions of the evolution in their surface drying state.

34

35   INTRODUCTION

36   Fugitive dust emissions emanating from mining residues can be a significant environmental

37   concern facing tailing storage facilities, challenging their prevention and mitigation efforts that, as

38   a result, become increasingly costly and labor intensive (Allan, 1995; Power, Gräfe, & Klauber,

39   2011). Unfortunately, forecasting and risk assessment efforts are hampered by our limited

40 understanding of the impact of meteorological conditions, as well as of mine tailings

41 microstructural and physicochemical properties, on their drying mechanisms and rates.

42   To tackle this problem, a bauxite residues storage area (BRSA) was selected as a case study

43 allowing meteorological records to be scrutinized in order to highlight the environmental

44 conditions that led to, and triggered, past fugitive dust emission events (Maurais et al., 2018). This

45 enabled the investigation of drying kinetics to be steered towards the most critical and relevant

46 environmental parameters for laboratory studies.   Numerous meteorological parameters are

47 continuously monitored by a weather station nearby the selected BRSA namely, wind speed and

48 direction, precipitations, as well as atmospheric temperature and relative humidity (RH).   This

49 latter was shown to be the most aggravating environmental parameter leading to dust particles

50 scattering events (Maurais et al., 2018). Therefore, thermal imaging techniques were brought to

51 bear on this issue by evaluating whether they could help quantify the evaporation kinetics of

52 bauxite residues. They are demonstrated herein to be convenient and effective tools for

53 investigation into evaporation rates that govern the drying process and to provide invaluable

54 insight into the underlying water transport mechanisms (Fuchs & Tanner, 1967; Pfister,

55 McDonnell, Hissler, & Hoffmann, 2010; Price, 1980).

56   Previously reported methods for measuring water contents, drying rates and evaporative fluxes

57 from porous media include frequency/time-domain reflectometry (Topp & Davis, 1985; Wang,

58 Xia, Wang, & Lu, 2012; Yu & Drnevich, 2004), dielectric permittivity measurements (Wang et

59 al., 2012), ground penetrating radar dielectric constant measurements (Van Dam, 2014), electrical

60 conductivity or resistivity (Brevik, Fenton, & Lazari, 2006; Sheets & Hendrickx, 1995), visual

61 inspection of the evolution of the drying front within the sample (Shokri, Lehmann, & Or, 2009;

62 Shokri & Or, 2011), heat-pulse probes (Bristow, 1998; Bristow, Campbell, & Calissendorff, 1993;

63   Hopmans, Šimunek, & Bristow, 2002), to name only but a few. Unfortunately, these methods

64   either lack the sensitivity or selectivity towards the surface layer, and/or cannot be easily deployed

65   for continuous in-situ monitoring and field applications (Amano & Salvucci, 1989). They are thus

66   unsuitable for the specific context of evaluating surface drying states and rates as part of risk

67   assessment protocols for dust emissions from BRSA. Thermal imaging techniques possess those

68   desirable attributes and may thus prove to be equally effective at probing drying kinetics under

69   controlled conditions in the laboratory, as well as providing a potentially powerful management

70   tool to characterize the evaporation rates from bauxite tailing surfaces at BRSA (Price, 1980).

71   Drying kinetics from porous materials are very complex, displaying contributions from a number

72   of different water transport mechanisms resulting in distinctive regimes and stages that all depend

73   sensitively on their water content, their microstructural and physicochemical properties, as well as

74   on environmental conditions (McKenna Neuman, Boulton, & Sanderson, 2009). Indeed, when the

75   water content is elevated, as in the early stages of drying, capillary flow is expected to dominate

76   water transport to the surface (a regime thereafter referred to as stage I) allowing large evaporation

77   fluxes from wet residues to be sustained (Neriah, Assouline, Shavit, & Weisbrod, 2014; Or,

78   Lehmann, Shahraeeni, & Shokri, 2006; Shahraeeni & Or, 2010; Teng, Zhang, Zhang, Zhao, &

79   Sheng, 2019; Thiery, Rodts, Weitz, & Coussot, 2017). Eventually, the rupture of the wetting layer

80   at the percolation threshold causes hydraulic discontinuity within the porous media (Moldrup,

81   Olesen, Komatsu, Schjønning, & Rolston, 2001). This shifts the limiting water transport

82   mechanism from capillary flow to gas phase diffusion thereby yielding a significant slowing down

83   of the evaporation rates (a regime thereafter referred to as stage II) (Griend & Owe, 1994; Or et

84   al., 2006; Saravanapavan & Salvucci, 2000). The water content at which the transition from stage

85   I to stage II occurs has been correlated to the microstructural features of the porous media (Shokri

86 & Or, 2011). Therefore, it is expected that the evaporation kinetics from bauxite tailings should

87 not only depend strongly on their water content, but also on their chemical composition, as well

88 as on their morphological and physicochemical properties, attributes that govern which water

89 transport mechanism should be most effective under specific meteorological conditions (i.e.,

90 temperature and relative humidity) (Saravanapavan & Salvucci, 2000). Given the role of capillary

91 forces in maintaining the cohesion of dust particles with tailing sites surfaces, forecasting of

92 fugitive dust emissions from BRSA depend most critically on a detailed quantitative understanding

93 of bauxite tailings evaporation kinetics as well as an the ability to predict their surface drying state

94 (Shao, 2001).

95   In this work, we describe how thermal imaging techniques enable evaporation rates from bauxite

96 residues to be quantified. This methodology should help describe, probe, understand, and predict

97 bauxite residues evaporation kinetics, as well as their dependence on environmental parameters

98 representative of those found at the BRSA (Neriah et al., 2014). Collectively, these investigations

99 should improve our ability to predict the drying state of bauxite residues surfaces, forecast and

100 prevent the occurrence of fugitive dust emissions, as well as devise efficient risk assessment and

101 monitoring tools to assist in mining residues management and environmental mitigation efforts.

102

103 MATERIALS AND METHODS

104   A methodology based on thermal imaging techniques was devised allowing for the

105 measurements of drying kinetics from porous media. The surface-sensitivity and selectivity of

106 optical methods (i.e., tens to a few hundreds of microns) enable measurements of surface

107 temperatures from mine tailings under controlled ambient temperature and relative humidity

108 conditions in the laboratory. Furthermore, the portability and ease of use of the commercial

109 infrared camera used in this work (FLIR® Model A320) are attractive features for field

110 applications. These may thus enable thermal imaging techniques to be brought to bear on real-time

111 monitoring of the evaporation process from the surface of mine tailings storage facilities.

112 Under given environmental conditions (i.e., ambient T and RH), water vapour concentration and

113 temperature gradients can establish rapidly in the superficial layers of evaporating porous media,

114 evolving continuously thereafter throughout the drying process. These gradients provide a driving

115 force for the long-range diffusive/convective transport of heat and water vapour, processes that are

116 required to sustain water evaporation from the samples surface, and that explain the strong

117 dependency of the drying kinetics on environmental parameters (Neriah et al., 2014). In addition,

118 it is thus also expected that the drying kinetics should depend strongly on sample thickness, as

119 well as on their microstructure and physico-chemical properties, in addition to their water content

120 (Grifoll, Gastó, & Cohen, 2005). Under quasi-steady state conditions (Monteith, 1981), equation

121 1 indicates that the surface temperatures observed for evaporating bauxite residues can be

122 understood by comparing the latent heat flux of evaporation from the samples surface (calculated

123 from the evaporation flux, J_{evap}, and the vaporization enthalpy, ΔH_{evap}) to the sensible heat flux

124 sustained by their thermal conductivity, K, through the gradient in their temperature depth-profile,

125 ∇T (Kosky, Balmer, Keat, & Wise, 2013):

$$K \cdot \nabla T = J_{evap} \cdot \Delta H_{evap} \qquad [1]$$

127 Therefore, surface temperature measurements can straightforwardly and directly inform on the

128 evaporative fluxes emanating from drying mine tailings. The magnitude of evaporative cooling at

129 the sample surface is reported using thermal imaging measurements of the difference in surface

130 temperatures (ΔT, with a precision of ± 30 mK) between drying bauxite residues samples and those

131 from reference samples. These latter are bauxite residues that have been let to reach equilibrium

132   with the environmental conditions, at the selected ambient temperature and relative humidity

133   (Monteith, 1981).

134   Evaporation kinetics from porous media also depend strongly on their water content along with

135   their physicochemical and morphological properties (Or et al., 2006). Indeed, at water contents

136   above a critical threshold value, capillary flow supplies the evaporating surface with liquid water

137   and is the dominant water transport mechanism that controls drying rates (Neriah et al., 2014).

138   This critical threshold volumetric water content, θ_{thr}, is defined by the minimal water content for

139   which long-range transport by solute diffusion in the liquid phase is possible (Moldrup et al., 2001;

140   Shokri & Or, 2011; Thiery et al., 2017). Below θ_{thr}, the hydraulic continuity is disrupted, and the

141   evaporation kinetics should thus become increasingly limited by water vapour diffusion from the

142   vaporisation front to the sample's surface (Moldrup et al., 2001). Therefore, θ_{thr} informs us on the

143   dominant transport mechanism likely to limit the evaporation of water and can be evaluated using

144   a non-linear empirical relationship that relates θ_{thr} with the specific surface area (SSA) of the

145   porous medium (Moldrup et al., 2001):

146                         $$\theta_{thr} = 0.039 \cdot SSA_{vol}^{0.52}$$ [2]

147   Equation 2 indicates that materials with large SSAs, such as bauxite residue (44-87 cm^2/g) (Li,

148   1998, 2001; Li & Rutherford, 1996), yield in an elevated value of θ_{thr} expressed as V_w/V_t, where

149   V_w is the volume of water and V_t the total volume of wet bauxite residues. Using the SSAs reported

150   in the literature (Li, 1998, 2001; Li & Rutherford, 1996) along with the macroscopic densities

151   measured for the bauxite residues used in the present study, $\rho_{bulk} = (1.2 \pm 0.1)$ g/cm^3, θ_{thr} is found

152   to vary between 31 % and 44 %, with an average value of (38 ± 4) % (V_w/V_t).

153   The bauxite residue samples, having reached different drying stages, were collected from various

154   locations at the selected BRSA. They were rinsed, dried and prepared with an initial solid fraction

7

of 70 % (m_b/m_t, where m_b is the mass of dry bauxite residues and m_t the total mass of wet bauxite residues), an initial drying state representative of the late stages of drying where fugitive dust emissions are most likely to occur. Furthermore, as it corresponds to an initial volumetric water content of 37 %, a contribution from capillary flow driven evaporation (i.e., stage I) is therefore likely to be observed in the early stages of the drying process for the experimental conditions explored in this work. Subsequently, gas phase water diffusion and adsorption on bauxite residues surfaces are expected to become the dominant mechanisms that should limit water transport from the vaporisation plane to the evaporating samples' surface (i.e., stage II).

In order to provide insight into the conditions under which the diffusive and/or capillary processes limit water transport to the surface and thus, the evaporation rate, sample holders with various depths, d = 2, 4, 6, and 8 mm, were used. These thicknesses encompass the critical superficial layers that are prone to dust scattering from BRSA surfaces. Surface temperature measurements were performed using compacted samples of wet bauxite residues until completion of water evaporation (i.e., when drying bauxite residues surface temperatures reach those of the reference sample, within the thermal imaging temperature measurements accuracy of ± 30 mK). Wet bauxite residues and reference samples were introduced in a controlled environmental chamber (Humidity test chamber; VWR® Model 9005L), maintained at a fixed temperature and ambient pressure (i.e., 310 K and 1 atm), and exposed to controlled relative humidity (RH) conditions of 35 %, 40 %, 50 %, 60 % and 70 %. The thermal camera was placed in the experimental chamber and was connected to a data processing software, allowing continuous and simultaneous measurements of the reference and wet bauxite residues surface temperatures to be performed for each sample thickness, as can been gleaned from the representative snapshots of a typical experimental time series reported in Figure 1.

178   Finally, water adsorption isotherms were performed using initially dry bauxite residue

179   samples that have been let to equilibrate with the environmental conditions (i.e., T = 310 K, P = 1

180   atm, at the selected RHs). Once thermodynamic equilibrium was reached between the bauxite

181   residue sample and the selected environmental conditions, the gain in mass of the sample due to

182   the adsorbed water mass (m_w) was determined using a high precision analytical balance enabling

183   their equilibrium water content to be measured.

184
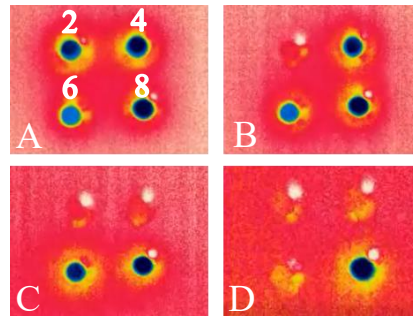
Figure 1. Snapshots from a time series showing thermal images of evaporating wet bauxite residue for sample thickness, d = 2 mm (top left), 4 mm (top right), 6 mm (bottom left) and 8 mm (bottom right) : as prepared **(A)**, and upon complete drying of the 2 mm **(B)**, 4 mm **(C)** and 6 mm **(D)** thick sample.
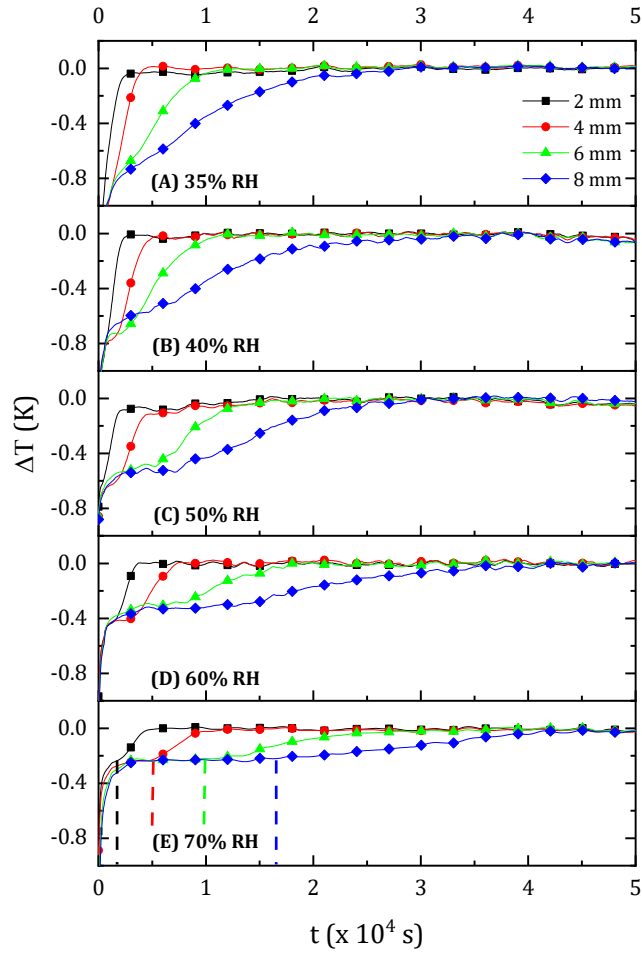
Figure 2. Evolution of the temperature difference (ΔT) between the sample and the reference surfaces during drying of bauxite residues prepared with an initial solid fraction of 70% (m_b/m_t) at T = 310 K. Sample thicknesses of 2 mm (black squares), 4 mm (red circles), 6 mm (green triangles) and 8 mm (blue diamonds) were monitored at a relative humidity of 35% (A), 40% (B), 50% (C), 60% (D) and 70% (E). The vertical lines in E indicate the onset of the transition from stage I to stage II evaporation regimes.

186 The evolution of the temperature difference between the bauxite residues and reference surfaces

187 (ΔT) as a function of time for sample thicknesses, d = 2, 4, 6, and 8 mm (black squares, red circles,

188 green triangle, and blue diamonds, respectively), at a selected relative humidity (RH = 35 %, 40

189 %, 50 %, 60 %, and 70 %, reported in Figure 2A, 2B, 2C, 2D, and 2E, respectively), reveals the

190 complex nature of bauxite residues drying kinetics. As expected, the evaporation rates depend

191 strongly, and in a non-linear way on d, indicating that long-range transport through the bauxite

192 residues porous microstructure must play an essential role in the drying process. Lower initial ΔT

193 values are observed for each RH in Figure 2, reported as $\Delta T_{free, evap.}$ increase from ~ -800 mK at 35

194 % RH to ΔT ~ -250 mK at 70 % RH appear to be conspicuously independent of d. This reveals

195 that the initial drying rates remain constant during stage I evaporation, and that they recede as the

196 ambient RH increases. This is most likely due to free water evaporation from wet bauxite residues

197 in their early stages of drying, a process that is sustained by rapid capillary flow from the bulk to

198 the surface (Or et al., 2006). As such, these initial ΔT value are reported as $\Delta T_{free, evap.}$ Figure 2

199 reveals that the duration of this capillary-driven free water evaporation regime increases with

200 sample thickness and that it decreases with increasing RH.

201 Stage I evaporation is followed by an evaporation regime where surface temperatures slowly

202 rise until the samples eventually reach thermal equilibrium with their environment. Indeed, as

203 water content in evaporating bauxite residues decreases, it compromises the hydraulic continuity

204 between the vaporisation plane, buried in the bulk of the sample, and their surface. Therefore,

205 during stage II evaporation, the surface temperatures gradually rises as the evaporation rates

206 become increasingly limited by the much slower diffusion of water vapour towards the sample

207 surface until ΔT tends asymptotically to zero (i.e., near-equilibrium conditions). As a result, the

208 dominant mechanism and rate-limiting process that sustains the evaporation flux from the samples

209 surface shifts from capillary flow (stage I) to diffusive water vapour transport (stage II). In Figure

210 2E, vertical dashed lines indicate the onset of the transition from stage I to stage II evaporation
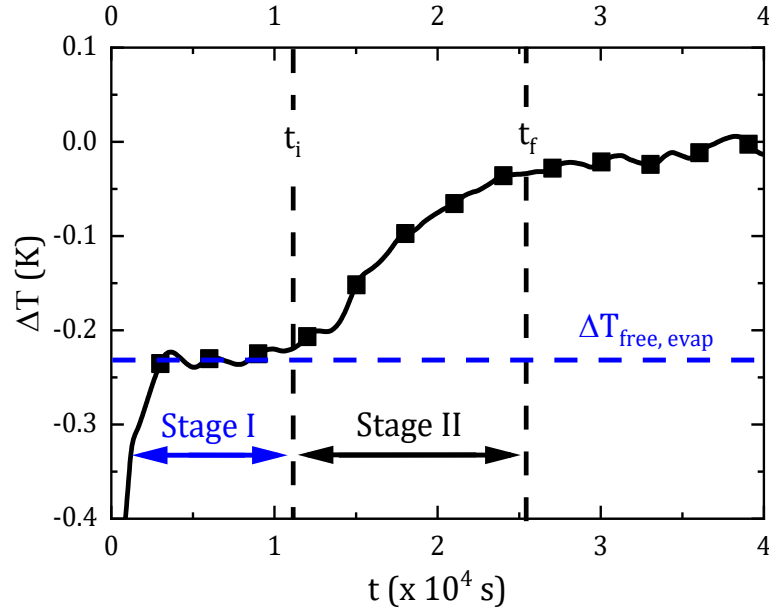

Figure 3. Evolution of the temperature difference (ΔT) between the sample and the reference surfaces during drying of a 6 mm thick bauxite residues sample with an initial solid fraction of 70% (m_b/m_t), at RH = 70% and T = 310 K. Stage I is characterised by a constant $\Delta T = \Delta T_{\text{free, evap.}}$ that is independent of d suggesting that free water evaporation from wet bauxite residue is sustained by rapid capillary flow. From the onset of stage II (at t = t_i), the surface temperature rises as evaporation becomes increasingly limited by slow gas phase diffusion until it reaches thermodynamic equilibrium (at t = t_f) with its environment at specific T and RH.

211 regimes for each sample thickness at 70% RH.

212   As drying kinetics slow down significantly with increasing RH, the distinct evaporation regimes

213 can be most clearly observed, described and analysed under these more elevated RH conditions.

214   Experimental data obtained from the 6 mm thick sample at RH = 70 % (Figure 2E, green trace) is

215   thus reproduced in Figure 3 in order to illustrate the most salient features used in the subsequent

216   discussions and analysis. The time at which surface temperatures increase to $\Delta T = \Delta T_{\text{free, evap.}} + 30$

217   mK is used to signal the onset of the smooth transition between the stage I and stage II evaporation

218   regimes and is indicated by the dashed vertical line labelled t_i, in Figure 3. Similarly, the diffusion-

219   limited stage II evaporation regime can be considered complete when $\Delta T = -30$ mK, as indicated

220   by the dotted vertical lines labelled t_f, in Figure 3. Using these somewhat arbitrary definitions, the

221   duration of the diffusion-limited stage II evaporation regime in the thermograms of Figure 2 is

222   observed to increase rapidly with sample thickness, and to decrease with RH.

223   At the end of stage II evaporation, bauxite residues samples reach a water content that should be

224   nearly equilibrated with the ambient RH at the temperature of 310 K. In order to determine the

225   water content within bauxite residues under equilibrium conditions, adsorption isotherm

226   measurements were performed at each relative humidity by studying water uptake by initially dry

227   bauxite residues samples (Figure 4). The adsorption isotherm indicates large water uptake by

228   bauxite residues under these equilibrium conditions as expected from their large SSA while an

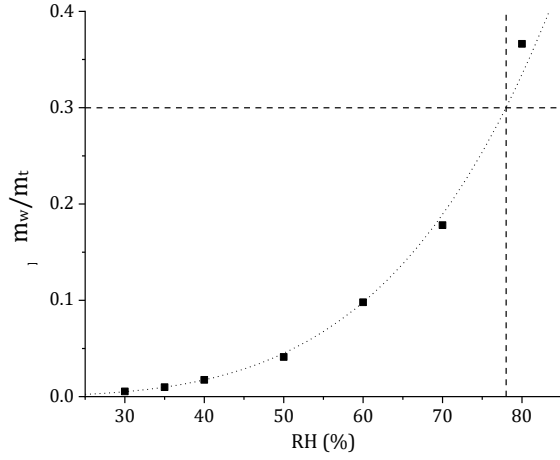229   important contribution must arise from their large microporosity.

Figure 4. Adsorption isotherm of initially dry bauxite residues acquired at different RH at T = 310 K. The dotted line is a guide to the eye. The dashed lines highlight the fact that the equilibrium water content reaches 30 % (m_w/m_t) at RH = 78 %.
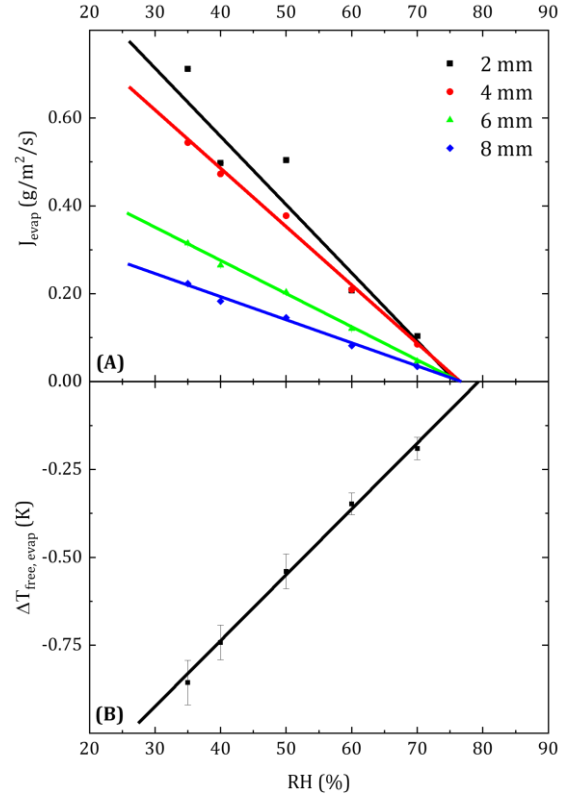

Figure 5. (A) Temperature difference in the initial stages of evaporation ($\Delta T_{free, evap.}$) as a function of relative humidity (RH). **(B)** Dependence of the average evaporation fluxes (J_{evap}) for each sample thickness [d = 2mm (black squares), 4mm (red circles), 6mm (green triangles), 8mm (blue diamonds)] as a function of relative humidity.

230   From the initial and equilibrium water contents, the loss of water experienced during the

231   evaporation process could be calculated. Using the total mass of water evaporated from the

232   samples, their total evaporation time (i.e., t_f), and the sample cross section (48 ± 2 mm²), the

233   average evaporation fluxes, J_{evap}, from the bauxite residue samples could be calculated at the

234   specific RH and d of each experiment (Figure 5A). Inspection of the dependence of J_{evap} on RH

235   for each sample thickness (i.e., d = 2, 4, 6, and 8 mm labeled by black squares, red circles, green

236   triangle, and blue diamonds, respectively) provides important phenomenological information. J_{evap}

237   decreases linearly with increasing RH and intercepts the x-axis at RH = (76 ± 4) % and that,

238   irrespective of the sample thickness. This indicates that the surface boundary conditions imposed

239   by the ambient RH levels control the evaporative flux and thus, the evaporation time. In addition,

240   the temperature difference due to free water evaporation in drying stage I ($\Delta T_{free, evap.}$), reported in

241   Figure 5B, follows a linear relationship with RH, in accord with expectations from equation 1, and

242   approaches zero when RH = (79 ± 4) %. The x-intercept values for Figure 5A and 5B are consistent

243   with the adsorption isotherm of Figure 4, where the dashed lines indicate that an equilibrium water

244   content of 30 % (m_w/m_t) is reached at RH = 78 %. Interestingly data from Figure 5A also reveals

245   that J_{evap} increases with decreasing d which can be explained by the fact that a larger fraction of

246   the water content lies at, or near, the surface of the thinner samples where free water evaporation

247   occurs, resulting in higher average drying rates. This dependence indicates that J_{evap} is not only

248   controlled by the boundary conditions, which depend on RH, but also by long-range vapour phase

249   diffusion which inhibits water transport from the vaporisation plane to the samples' surface,
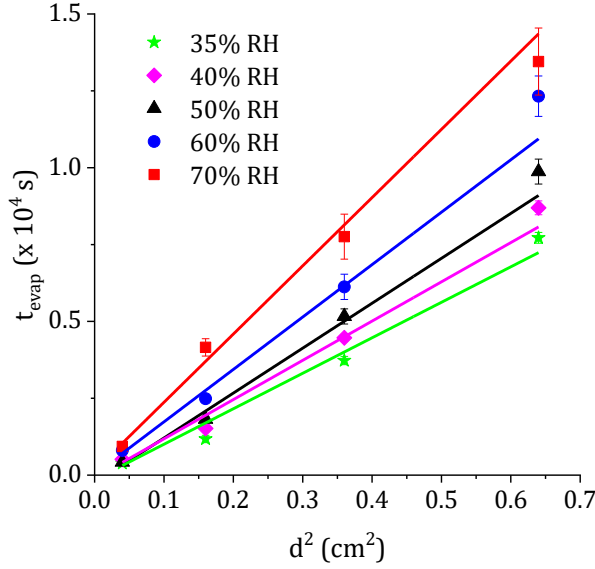
250   through the depleted evaporated interfacial zone.

Figure 6. Stage II evaporation half-time (t_{evap}) as a function of the sample thickness squared (d^2) for RH = 35 % (green star), 40 % (magenta diamond), 50 % (black triangles), 60 % (blue circles), 70 % (red squares).
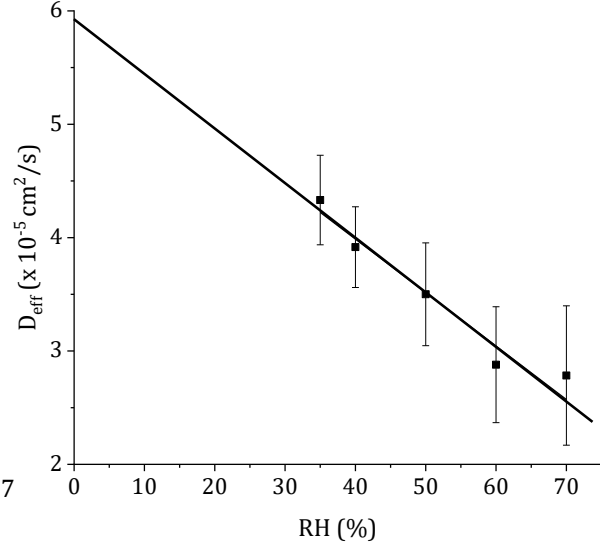
Figure 7. Dependence of the effective diffusion coefficient (D_{eff}) on the relative humidity (RH) at T = 310 K.

251   As stage II of the drying process is interpreted as being diffusion-limited, it is expected to follow

252   Fick's law and to display an effective diffusion coefficient (D_{eff}). Diffusive transport would imply

253   a linear dependence between diffusion time and the mean squared displacement of diffusing

254   molecules whose slope could reveal the effective diffusion coefficient (D_{eff}), following $t_{evap} =$

255    $\frac{d^2}{2D_{eff}}$, assuming 1D diffusive transport within the bauxite residues samples. Equating the mean

256   squared displacement of diffusing molecules to the sample thickness [i.e., $\langle z^2 \rangle \sim d^2$], and using

257   the stage II evaporation half-time (t_{evap}, defined here as $\frac{t_f - t_i}{2}$, using t_f and t_i as defined and

258   displayed in Figure 3), Figure 6 shows that indeed, a linear relationship between t_{evap} and d^2 is

259   obeyed. In addition to corroborating the diffusive nature of the rate limiting process for water

260   evaporation in late stage drying, an effective diffusion coefficient for water in bauxite residues can

261   be obtained using linear fits to the experimental data in Figure 6.

262   The effective diffusion coefficients obtained at each RH are reported in Figure 7 and,

263   interestingly, they decrease rapidly with increasing RH. Furthermore, these effective diffusion

264   coefficients are four orders of magnitude smaller than those commonly measured for gas phase

265   diffusion (Jabro, 2009). This must therefore reflect the fact that water diffusion is hindered by the

266   microstructure and water adsorption propensity of the medium, properties that diminish the

267   effective diffusion coefficient through the interstitial air within the bauxite residues interconnected

268   porous microstructure. Indeed, when diffusive transport occurs in porous media, D_{eff} can be

269   described using the molecular diffusion coefficient in air (D_{air}), the porosity of the sample (φ =

270   0.64 ± 0.06) and the tortuosity of its pore structure (τ = 1.38 ± 0.07) (Ho & Webb, 2006).

271   Contributions arising from adsorption of water on pore surfaces are described using parameters

272   that account for the water/bauxite residues interactions, namely an equilibrium constant for

273   adsorption (K_{ads}), for the bauxite residues mass-to-pore volume ratio (r_{sp} = 0.7 ± 0.1 g/cm^3) and

274   their specific surface area [$SSA = (5 \pm 1) \times 10^5$ cm^2/g] (Bartels-Rausch et al., 2013; Fabre, Barnola,

275   Arnaud, & Chappellaz, 2000; Schwander et al., 1993; Seok et al., 2009):

$$D_{eff} = D_{air} \cdot \left(\frac{\varphi}{\tau}\right) \cdot \left(\frac{1}{1+ r_{sp} \times K_{ads} \times SSA}\right) \tag{3}$$

277   Equation 3 also provides a framework to understand the dependence of D_{eff} with RH. As the

278   vaporisation plane leaves the surface of the bauxite residues, the overlying depleted zone, which

279   remains in a quasi-steady state with the environmental conditions, acts as a diffusion barrier. When

280   the RH increases, the water content in the evaporated interfacial layer, which is in a dynamic

281   equilibrium with ambient air temperature and relative humidity, also increases. Consequently, the

282 air-filled porosity decreases, and the tortuosity of the pore structure increases, yielding a decrease

283 in D_{eff} with increasing RH as observed in Figure 7.

284 Given that the morphological parameters, φ and τ, can only account for an utmost factor of

285 $\frac{\varphi}{\tau} \sim 0.5$ reduction in D_{eff} compared to D_{air}, water adsorption on bauxite residue surfaces appears

286 to be crucial in order to explain the smallness of D_{eff}. While SSA, r_{sp}, φ, and τ values are well

287 established for dry bauxite residues (i.e., 0 % m_w/m_t), the equilibrium constant for adsorption,

288 K_{ads}, for water for this material is unfortunately still unknown. A linear extrapolation of D_{eff}

289 with RH enables the diffusion coefficient of water in dry bauxite residues to be estimated as D_{eff}

290 = (5.9 ± 0.3) x 10^{-5} cm^2/s at RH = 0 %. Using Equation 3, along with the known morphological

291 parameters of dry bauxite residues, a value for K_{ads} = (5 ± 1) x 10^{-3} cm is obtained. The magnitude

292 of K_{ads} for bauxite tailings is observed to be greater than those reported for loam soils and alumina

293 active F-200 for example, that is (6 ± 1) x 10^{-4} cm (Gary, Kohl, & Taylor, 1964) and (6.6 ± 0.9) x

294 10^{-5} cm (Serbezov, 2003), respectively. Therefore, water vapour strong propensity towards

295 adsorption onto bauxite residues pore surfaces, along with their large SSA, are suggested to be the

296 dominant contributors to the large decrease of D_{eff} compared to D_{air}, and the slow drying kinetics

297 displayed in stage II evaporation regime.

298

299 CONCLUSIONS

300 Thermal imaging was demonstrated to be an efficient and innovative tool for monitoring

301 surface evaporation from bauxite residues and establishing the underlying drying mechanisms. A

302 thorough analysis of the experimental data enabled a deeper understanding of the evaporation

303 kinetics and effective diffusion coefficients to be quantified. Water adsorption on bauxite residues

304 is demonstrated to be the dominant phenomenon in the rate-limiting mechanism in the later

305 evaporation stage and to be responsible for the smallness of the effective diffusion coefficient. The

306 evaporated interfacial layers therefore act as a diffusion barrier to water transport from the

307 vaporization plane in the deeper layers of the bauxite residues to their surface, inhibiting

308 considerably their drying rates.

309   A limitation of the thermal imaging approach is that it can only provide average evaporation

310 fluxes. Indeed, as soon as the vaporization plane leaves the sample surface, contributions from the

311 thermal gradient through the bauxite residues temperature depth profile arise, preventing

312 instantaneous drying rates to be established and finer details in the evolution of the dominant water

313 transport mechanisms to be elucidated. Concomitant gravimetric and thermal imaging

314 measurements should provide us with further valuable mechanistic insight.

315   This methodology could also be expanded to environmental conditions relevant to field

316 applications, namely the temperature dependence of the drying kinetics, especially those

317 encountered under Winter conditions where capillary transport will be strongly suppressed

318 (Feddes, Kabat, Van Bakel, Bronswijk, & Halbertsma, 1988). Environmental mitigation efforts

319 could benefit greatly from improved understanding of the drying rates under such Winter condition

320 where acute environmental consequences result from dust particles scattering from BRSA over

321 snow-covered neighbouring urban communities (Aoki et al., 2006; Warren & Wiscombe, 1980).

322 Collectively, these investigations should improve our ability to forecast and prevent the occurrence

323 of fugitive dust emissions as well as to devise efficient risk assessment and monitoring tools to

324 assist in mining residue management efforts.

325

326

335

336

337

338

339   AUTHOR INFORMATION

340   **Corresponding Author**

341   Josée Maurais: Josee.Maurais@USherbrooke.ca

342

343

344

345

346
347

348

349

350   REFERENCES

351

352   Allan, R. J. (1995). Impact of Mining Activities on the Terrestrial and Aquatic Environment with

353   Emphasis on Mitigation and Remedial Measures. In U. Förstner, W. Salomons, & P. Mader

354   (Eds.), *Heavy Metals* (pp. 119–140). Springer, Berlin, Heidelberg.

355   https://doi.org/10.1007/978-3-642-79316-5_8

356   Amano, E., & Salvucci, G. D. (1989). Detection and Use of Three Signatures of Soil-Limited

357   Evaporation. *Remote Sensing of Environment*, *4257*(98).

358   Aoki, T., Motoyoshi, H., Kodama, Y., Yasunari, T. J., Sugiura, K., & Kobayashi, H. (2006).

359   Atmospheric Aerosol Deposition on Snow Surfaces and Its Effect on Albedo. *SOLA*, *2*, 13–

360   16. https://doi.org/10.2151/sola.2006-004

361   Bartels-Rausch, T., Wren, S. N., Schreiber, S., Riche, F., Schneebeli, M., & Ammann, M. (2013).

362   Diffusion of volatile organics through porous snow: impact of surface adsorption and grain

363   boundaries. *Atmospheric Chemistry and Physics*, *13*(14), 6727–6739.

364   https://doi.org/10.5194/acp-13-6727-2013

365   Brevik, E. C., Fenton, T. E., & Lazari, A. (2006). Soil electrical conductivity as a function of soil

366   water content and implications for soil mapping. *Precision Agriculture*, *7*(6), 393–404.

367   https://doi.org/10.1007/s11119-006-9021-x

368   Bristow, K. L. (1998). Measurement of thermal properties and water content of unsaturated sandy

369   soil using dual-probe heat-pulse probes. *Agricultural and Forest Meteorology*, *89*(2), 75–84.

370   https://doi.org/10.1016/S0168-1923(97)00065-8

371 Bristow, K. L., Campbell, G. S., & Calissendorff, K. (1993). Test of a Heat-Pulse Probe for
372   Measuring Changes in Soil Water Content. *Soil Science Society of America Journal*, *57*, 930–
373   934. https://doi.org/10.2136/sssaj1993.03615995005700040008x

374 Fabre, A., Barnola, J.-M., Arnaud, L., & Chappellaz, J. (2000). Determination of gas diffusivity in
375   polar firn: Comparison between experimental measurements and inverse modeling.
376   *Geophysical Research Letters*, *27*(4), 557–560. https://doi.org/10.1029/1999GL010780

377 Feddes, R. A., Kabat, P., Van Bakel, P. J. T., Bronswijk, J. J. B., & Halbertsma, J. (1988).
378   Modelling soil water dynamics in the unsaturated zone — State of the art. *Journal of*
379   *Hydrology*, *100*(1), 69–111. https://doi.org/10.1016/0022-1694(88)90182-5

380 Fuchs, M., & Tanner, C. B. (1967). Evaporation from a Drying Soil. *Journal of Applied*
381   *Meteorology*, *6*(5), 852–857. https://doi.org/10.1175/1520-
382   0450(1967)006<0852:EFADS>2.0.CO;2

383 Gary, J. W., Kohl, R. A., & Taylor, S. A. (1964). Water Adsorption by Dry Soil and Its
384   Thermodynamic Functions. *Soil Science Society Proceedings*, *28*(3), 309–314.
385   https://doi.org/doi:10.2136/sssaj1964.03615995002800030007x

386 Griend, A. A., & Owe, M. (1994). Bare soil surface resistance to evaporation by vapor diffusion
387   under semiarid conditions. *Water Resources Research*, *30*(2), 181–188.
388   https://doi.org/10.1029/93WR02747

389 Grifoll, J., Gastó, J. M., & Cohen, Y. (2005). Non-isothermal soil water transport and evaporation.
390   *Advances in Water Resources*, *28*(11), 1254–1266.
391   https://doi.org/10.1016/j.advwatres.2005.04.008

392   Ho, C. K., & Webb, S. W. (2006). *Gas Transport in Porous Media*. Springer Netherlands.

393   https://doi.org/10.1007/1-4020-3962-X

394   Hopmans, J. W., Šimunek, J., & Bristow, K. L. (2002). Indirect estimation of soil thermal

395   properties and water flux using heat pulse probe measurements: Geometry and dispersion

396   effects. *Water Resources Research*, *38*(1), 7–14. https://doi.org/10.1029/2000WR000071

397   Jabro, J. D. (2009). Water Vapor Diffusion Through Soil as Affected by Temperature and

398   Aggregate Size. *Transport in Porous Media*, *77*(3), 417–428. https://doi.org/10.1007/s11242-

399   008-9267-z

400   Kosky, P., Balmer, R., Keat, W., & Wise, G. (2013). Chapter 12 - Mechanical Engineering. In P.

401   Kosky, R. Blamer, W. Keat, & G. Wise (Eds.), *Exploring Engineering* (Third Edit, pp. 259–

402   281). Boston: Academic Press. https://doi.org/10.1016/B978-0-12-415891-7.00012-1

403   Li, L. Y. (1998). Properties of red mud tailings produced under varying process conditions. *Journal*

404   *of Environmental Engineering*, *124*(3), 254–264. https://doi.org/10.1061/(ASCE)0733-

405   9372(1998)124:3(254)

406   Li, L. Y. (2001). A study of iron mineral transformation to reduce red mud tailings. *Waste*

407   *Management*, *21*(6), 525–534. https://doi.org/10.1016/S0956-053X(00)00107-0

408   Li, L. Y., & Rutherford, G. K. (1996). Effect of bauxite properties on the settling of red mud.

409   *International Journal of Mineral Processing*, *48*(3–4), 169–182.

410   https://doi.org/10.1016/S0301-7516(96)00024-5

411   Maurais, J., Bourret, J., Dauphinais, E., Larivière-Loiselle, C., Beaumont, É., Morin, É., … Ayotte,

412   P. (2018). Prevention And Mitigation Of Fugitive Dust Emission From Bauxite Residue:

413   Aggravating Environmental Effects, Forecasting And Risk Assessment. In *Alumina Quality*

414   *Workshop (AQW) 2018*. Gladstone: Alumina Quality Workshop (AQW).

415   McKenna Neuman, C., Boulton, J. W., & Sanderson, S. (2009). Wind tunnel simulation of

416   environmental controls on fugitive dust emissions from mine tailings. *Atmospheric*

417   *Environment*, *43*(3), 520–529. https://doi.org/10.1016/j.atmosenv.2008.10.011

418   Moldrup, P., Olesen, T., Komatsu, T., Schjønning, P., & Rolston, D. E. (2001). Tortuosity,

419   Diffusivity, and Permeability in the Soil Liquid and Gaseous Phases. *Soil Science Society of*

420   *America Journal*, *65*, 613–623. https://doi.org/10.2136/sssaj2001.653613x

421   Monteith, J. L. (1981). Evaporation and surface temperature. *Quarterly Journal of the Royal*

422   *Meteorological Society*, *107*(451), 1–27. https://doi.org/10.1002/qj.49710745102

423   Neriah, A. Ben, Assouline, S., Shavit, U., & Weisbrod, N. (2014). Impact of ambient conditions

424   on evaporation from porous media. *Water Resources Research*, *50*(8), 6696–6712.

425   https://doi.org/10.1002/2014WR015523

426   Or, D., Lehmann, P., Shahraeeni, E., & Shokri, N. (2006). Advances in Soil Evaporation Physics

427   — A Review. *Vadose Zone Journal*, *12*(4). https://doi.org/10.2136/vzj2012.0163

428   Pfister, L., McDonnell, J. J., Hissler, C., & Hoffmann, L. (2010). Ground-based thermal imagery

429   as a simple, practical tool for mapping saturated area connectivity and dynamics.

430   *Hydrological Processes*, *24*(21), 3123–3132. https://doi.org/10.1002/hyp.7840

431   Power, G., Gräfe, M., & Klauber, C. (2011). Bauxite residue issues: I. Current management,

432   disposal   and   storage   practices.   *Hydrometallurgy*,   *108*(1–2),   33–45.

433   https://doi.org/10.1016/j.hydromet.2011.02.006

434   Price, J. C. (1980). The potential of remotely sensed thermal infrared data to infer surface soil

435   moisture and evaporation. *Water Resources Research*, *16*(4), 787–795.

436   https://doi.org/10.1029/WR016i004p00787

437   Saravanapavan, T., & Salvucci, G. D. (2000). Analysis of rate-limiting processes in soil

438   evaporation with implications for soil resistance models. *Advances in Water Resources*, *23*,

439   493–502. https://doi.org/10.1016/S0309-1708(99)00045-7

440   Schwander, J., Barnola, J.-M., Andrié, C., Leuenberger, M., Ludin, A., Raynaud, D., & Stauffer,

441   B. (1993). The age of the air in the firn and the ice at Summit, Greenland. *Journal of*

442   *Geophysical Research: Atmospheres*, *98*(D2), 2831–2838.

443   https://doi.org/10.1029/92JD02383

444   Seok, B., Helmig, D., Williams, M. W., Liptzin, D., Chowanski, K., & Hueber, J. (2009). An

445   automated system for continuous measurements of trace gas fluxes through snow: an

446   evaluation of the gas diffusion method at a subalpine forest site, Niwot Ridge, Colorado.

447   *Biogeochemistry*, *95*(1), 95–113. https://doi.org/10.1007/s10533-009-9302-3

448   Serbezov, A. (2003). Adsorption Equilibrium of Water Vapor on F-200 Activated Alumina.

449   *Journal of Chemical & Engineering Data*, *48*(2), 421–425.

450   https://doi.org/10.1021/je025616d

451   Shahraeeni, E., & Or, D. (2010). Thermo-evaporative fluxes from heterogeneous porous surfaces

452   resolved by infrared thermography. *Water Resources Research*, *46*(9).

453   Shao, Y. (2001). A model for mineral dust emission. *Journal of Geophysical Research:*

454   *Atmospheres*, *106*(D17), 20239–20254. https://doi.org/10.1029/2001JD900171

455   Sheets, K. R., & Hendrickx, J. M. H. (1995). Noninvasive Soil Water Content Measurement Using

456   Electromagnetic Induction. *Water Resources Research*, *31*(10), 2401–2409.

457   https://doi.org/10.1029/95WR01949

458   Shokri, N., Lehmann, P., & Or, D. (2009). Critical evaluation of enhancement factors for vapor

459   transport through unsaturated porous media. *Water Resources Research*, *45*, 1–9.

460   https://doi.org/10.1029/2009WR007769

461   Shokri, N., & Or, D. (2011). What determines drying rates at the onset of diffusion controlled

462   stage-2 evaporation from porous media? *Water Resources Research*, *47*, 1–8.

463   https://doi.org/10.1029/2010WR010284

464   Teng, J., Zhang, X., Zhang, S., Zhao, C., & Sheng, D. (2019). An analytical model for evaporation

465   from unsaturated soil. *Computers and Geotechnics*, *108*, 107–116.

466   https://doi.org/10.1016/j.compgeo.2018.12.005

467   Thiery, J., Rodts, S., Weitz, D. A., & Coussot, P. (2017). Drying regimes in homogeneous porous

468   media from macro- to nanoscale. *Phys. Rev. Fluids*, *2*(7), 74201.

469   https://doi.org/10.1103/PhysRevFluids.2.074201

470   Topp, G. C., & Davis, J. L. (1985). Measurement of Soil Water Content using Time-domain

471   Reflectrometry (TDR): A Field Evaluation. *Soil Science Society of America Journal*, *49*, 19–

472   24. https://doi.org/10.2136/sssaj1985.03615995004900010003x

473   Van Dam, R. L. (2014). Calibration Functions for Estimating Soil Moisture from GPR Dielectric

474   Constant Measurements. *Communications in Soil Science and Plant Analysis*, *45*(3), 392–

475   413. https://doi.org/10.1080/00103624.2013.854805

476   Wang, J. C., Xia, Z. Q., Wang, J. X., & Lu, Z. H. (2012). Field Evaluation of 12 Soil Moisture

477   Sensors on a Sandy Loam Soil in Lu'an, Subtropical Monsoon Climate Region, China.

478   *Advanced Materials Research*, *482–484*, 372–375.

479   https://doi.org/10.4028/www.scientific.net/AMR.482-484.372

480   Warren, S. G., & Wiscombe, W. J. (1980). A Model for the Spectral Albedo of Snow. II: Snow

481   Containing Atmospheric Aerosols. *Journal of the Atmospheric Sciences*, *37*(12), 2734–2745.

482   https://doi.org/10.1175/1520-0469(1980)037<2734:AMFTSA>2.0.CO;2

483   Yu, X., & Drnevich, V. P. (2004). Soil Water Content and Dry Density by Time Domain

484   Reflectometry. *Journal of Geotechnical and Geoenvironmental Engineering*, *130*(9), 922–

485   934. https://doi.org/10.1061/(ASCE)1090-0241(2004)130:9(922)

486